MNRAS **000**, 1–4 (2019) Preprint 30 September 2019 Compiled using MNRAS LATEX style file v3.0

Cassini State Capture

Yubo Su[1], Dong Lai[1]
[1] *Cornell Center for Astrophysics and Planetary Science, Department of Astronomy, Cornell University, Ithaca, NY 14853, USA*

Accepted XXX. Received YYY; in original form ZZZ

ABSTRACT
Abstract

Key words: planet–star interactions

1 INTRODUCTION

2 EQUATIONS

Denote $\vec{S}$ spin of planet, $\vec{l}$ angular momentum of planet, and $\vec{l}_d$ angular momentum of the surrounding disc. We approximate $S \ll L \ll L_d$, so $\vec{l}_d$ is approximately constant. Much of this treatment borrows from (Anderson & Lai 2018). We consider equations in the corotating frame

$$\frac{\mathrm{d}\hat{s}}{\mathrm{d}t} = \omega_{sl}\left(\hat{s}\cdot\hat{l}_d\right)\left(\hat{s}\times\hat{l}_d\right), \tag{1}$$

$$\frac{\mathrm{d}\hat{l}}{\mathrm{d}t} = \omega_{ld}\left(\hat{l}\cdot\hat{l}_d\right)\left(\hat{l}\times\hat{l}_d\right), \tag{2}$$

$$\omega_{sl} = \frac{3k_q}{2k}\left(\frac{R_1}{a_1}\right)^3 S, \tag{3}$$

$$\omega_{ld} = \dots. \tag{4}$$

(TODO get ω_{ld} from Millhollard & Batygin).

We go to the corotating frame with $\vec{l}$ such that it is also fixed in time. The evolution of $\hat{s}$ in this corotating frame is governed by:

$$\frac{\mathrm{d}\hat{s}}{\mathrm{d}t} = \alpha\left(\hat{s}\cdot\hat{l}\right)\left(\hat{s}\times\hat{l}\right) - |g|\left(\hat{s}\times\hat{l}_d\right). \tag{5}$$

$\alpha = \omega_{sd} > 0, g \equiv -\omega_{ld}\cos I < 0$ follow traditional sign conventions.

We divide through by α and define parameter η and nondimensionalized time τ

$$\eta \equiv \frac{|g|}{\alpha}, \tag{6}$$

$$\tau \equiv \alpha t. \tag{7}$$

Following Millholland & Batygin (2019), we allow g to vary in time owing to a disk with decaying mass

$$M_d(t) = M_d(0)e^{-t/t_d}. \tag{8}$$

As α is held constant, this equates to η decaying as $\frac{\mathrm{d}\eta}{\mathrm{d}t} = -\frac{\eta}{t_d}$ for some decay time t_η. We nondimensionalize by defining $\epsilon \equiv \frac{1}{\alpha t_\eta}$, so

$$\frac{\mathrm{d}\eta}{\mathrm{d}\tau} = -\epsilon\eta. \tag{9}$$

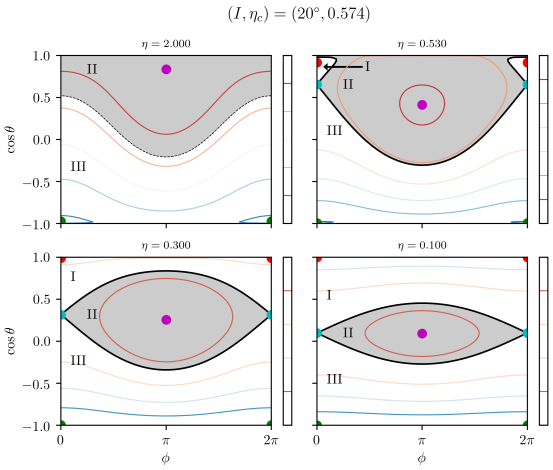

Figure 1. Contour plot of $H(\phi, \cos\theta)$. Black dotted line is the separatrix, which only exists for $\eta < \eta_c$.

2.1 Cassini States

The Cassini state Hamiltonian in the frame corotating with $\hat{l}_d$ about $\hat{l}$ is:

$$H = -\frac{1}{2}\left(\hat{s}\cdot\hat{l}\right)^2 + \eta\left(\hat{s}\cdot\hat{l}_d\right). \tag{10}$$

Spin states satisfying $\frac{\mathrm{d}\hat{s}}{\mathrm{d}t} = 0$ are referred to as *Cassini States* (CS). When $\eta < \eta_c$, there are four CSs, and when $\eta > \eta_c$ there are only two; η_c is (Henrard & Murigande 1987; Ward & Hamilton 2004)

$$\eta_c \equiv \left(\sin^{2/3} I + \cos^{2/3} I\right)^{3/2}. \tag{11}$$

CSs 1, 2, 3 are stable while CS4 is unstable. A contour plot of $H(\phi, \cos\theta)$ is

The locations of the $\cos\theta$ of the two/four CSs as a function of η is provided in

2.2 Separatrix

In the four-CS regime, one of the CSs is a saddle point, conventionally denoted Cassini State 4 (CS4). All trajectories are periodic

[t]

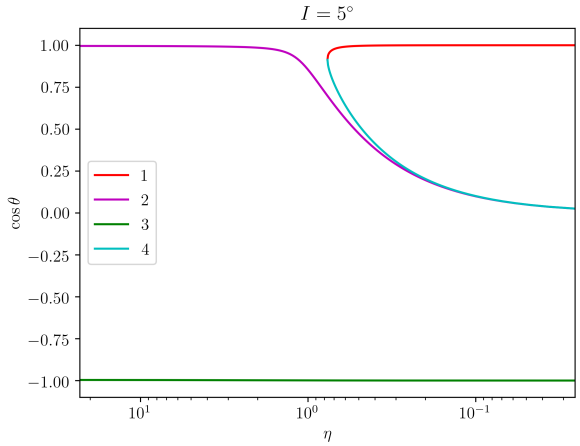

Figure 2. Locations of the Cassini states over time, following the same coloring scheme as Figure 1.

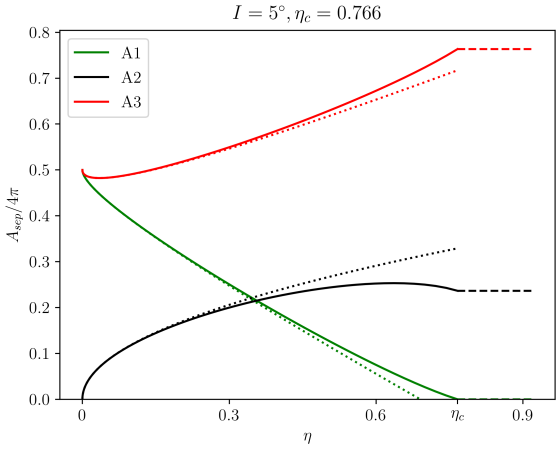

Figure 3. Plot of $A_i(\eta)$ as given by Equation 12. Dotted lines correspond to small η approximations discussed in Section C.

with finite period except two critical trajectories asymptotic in the past and future to CS4. Together, these two critical trajectories are referred to as the *separatrix* and divide phase space into three zones. We use notation described in Figure 1.

The unsigned area enclosed by the separatrix is known exactly in literature (Henrard & Murigande 1987; Ward & Hamilton 2004):

$$z_0 = \eta \cos I,$$

$$\chi = \sqrt{-\frac{\tan^3\theta_4}{\tan I} - 1},$$

$$\rho = \chi \frac{\sin^2\theta_4 \cos\theta_4}{\chi^2 \cos^2\theta_4 + 1},$$

$$T = 2\chi \frac{\cos\theta_4}{\chi^2 \cos^2\theta_4 - 1},$$

$$A_{II} = 8\rho + 4 \arctan T - 8 z_0 \arctan \frac{1}{\chi}, \tag{12a}$$

$$A_I = 2\pi (1 - z_0) - \frac{A_2}{2}, \tag{12b}$$

$$A_{III} = 2\pi (1 + z_0) - \frac{A_2}{2}. \tag{12c}$$

These are plotted as a function of η in Figure 3.

3 ADIABATIC EVOLUTION

In the truly adiabatic limit, $\epsilon \to 0$; we use $\epsilon = 3 \times 10^{-4}$ in subsection 3.1 and vary ϵ in subsection 3.2. The adiabatic limit is quantified in Millholland & Batygin (2019) to be

$$\dot{\eta} \lesssim \dots \tag{13}$$

3.1 Individual Simulations

In the limit $\eta \to 0$, all trajectories circulate with constant

$$\theta_f \equiv \left[\arccos \hat{s} \cdot \hat{l}\right]_{\eta \to 0}. \tag{14}$$

We run simulations that terminate at $\eta = 10^{-5}$ and measure θ_f. We vary the initial

$$\theta_{sd,i} \equiv \left[\arccos \hat{s} \cdot \hat{l}_d\right]_{t=0}. \tag{15}$$

Initially, in the $\eta > \eta_c$ regime, only zones II, III exist. Conversely, at the end of the simulation when $\eta \to 0$, only zones I, III exist. Naively then, one might expect four sequences of transitions between zones ("zone transition histories") to appear during simulations: (i) $II \to I$, (ii) $II \to III$, (iii) $III \to I$, and (iv) the trivial $III \to III$ where the trajectory never encounters the separatrix. In fact, (v) a fifth possible history involving two transitions is observed $III \to II \to I$.

Between zone transitions, the adiabatic invariant $J \equiv \oint \cos\theta \, \mathrm{d}\phi$ is conserved. Here, we adopt convention J is a *signed* area

$$J = \oint (1 - \cos\theta) \, \mathrm{d}\phi. \tag{16}$$

This has the advantage of (i) having a removable singularity when the trajectory crosses $\cos\theta = 1$, and (ii) being easily expressible as combinations of the A_i of Equation 12 without 2π offsets.

Given this definition, the change in J during a separatrix encounter is easily understood (Henrard 1982). We present in Figure 4 a fiducial simulaiton undergoing the $II \to I$ zone transition. An initial condition in zone II with initial adiabatic invariant $J_i > 0$ librates about CS2 until $A_{II} = J_i$. At this point, it encounters the separatrix and moves into zone I with $J_f = -A_I$. Further simulations illustrating the other zone transition histories are depicted in Section A.

3.2 Dynamical Outcomes

In the adiabatic limit, while separatrix encounters induce discontinuous changes in enclosed phase space, the outcomes of these encounters are well understood in pioneering work by Henrard (Henrard 1982; Henrard & Murigande 1987). For a wide range of $\theta_{sd,i}$, we run simulations over a ring of initial conditions at each $\theta_{sd,i}$ and measure the final θ_f values. We can also predict the values of θ_f for each of the dynamical histories as well as their associated probabilities; refer to Section C for details.

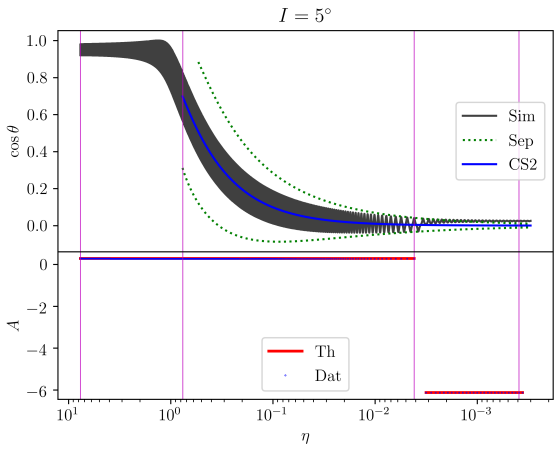

(a) Top: Plot of $\cos\theta(t)$ (grey) over an example simulation. Overlaid are the locations of Cassini State 2 (blue), upper and lower bounds on the separatrix (dashed green), and value of θ_f predicted in the adiabatic limit (horizontal red line). Bottom: Plot of the enclosed separatrix area obtained by integrating the simulated trajectory (blue dots) and fully adiabitic theory (red line). A small blip in the data area arises when the integration area crosses the coordinate singularity at the pole. Vertical red magenta lines denote the four snapshots depicted below; they correspond to the start of the simulation, the appearance of the separatrix, the separatrix encounter and the end of the simulation.

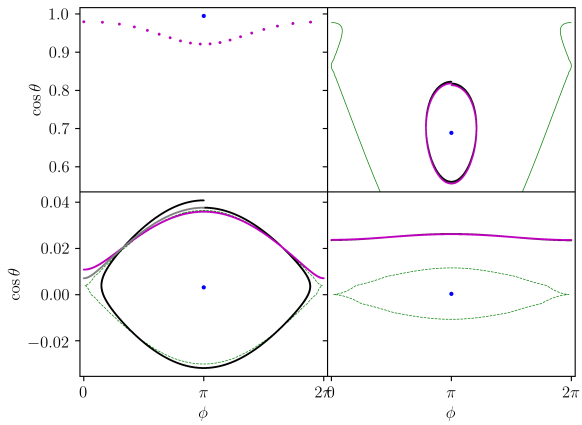

(b) Snapshots in the $(\cos\theta, \phi)$ space of the simulation trajectories for two circulation/libration cycles around the η values depicted above. Cycles are defined by the range of integration used to compute enclosed phase space area. Black dots denote the cycle immediately before the selected η value, magenta dots the cycle immediately after, and grey denotes intermediate points that do not constitute a full cycle. Also labeled are the separatrix (green) and Cassini State 2 (blue).

Figure 4. Fiducial simulation following the $A_2 \rightarrow A_1$ transition.

4 NONADIABATIC EVOLUTION

Here, we consider ϵ sufficiently large to violate the adiabiticity constraint Equation 13.

4.1 Sample Trajectory

A sample trajectory following in the style of Figure 4 but for $\epsilon = 0.1$ is provided in Figure 6.

4.2 Dynamical Outcomes

A formula for θ_f assuming $\theta_{sd,i} = 0$ initially can be given:

$$\theta_f\left(\theta_{sd,i} = 0\right) = \sqrt{\frac{2\pi\Omega}{\epsilon}} \tan I. \tag{17}$$

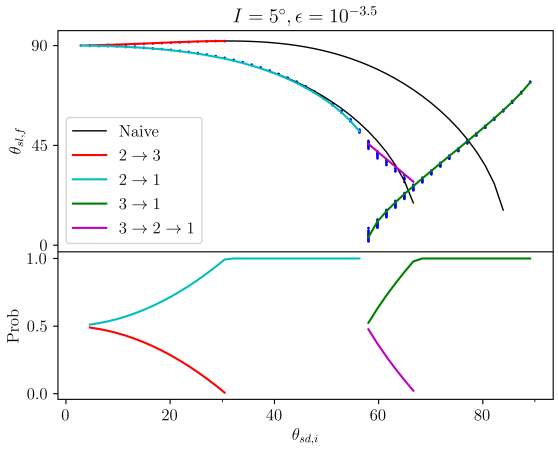

Figure 5. Top: $\theta_f\left(\theta_{sd,i}\right)$, overlaid with semi-analytic predictions of the θ_f for each of the four nontrivial dynamical histories in colored lines. Bottom: Semi-analytic probabilities of each of the dynamical histories for each $\theta_{sd,i}$.

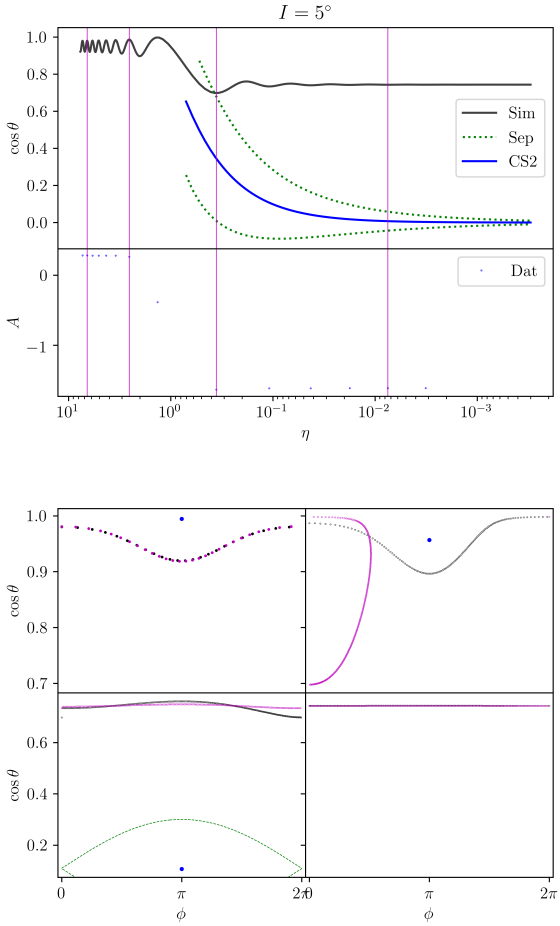

Figure 6. Same as Figure 6 but for a non-adiabatic $\epsilon = 0.1$.

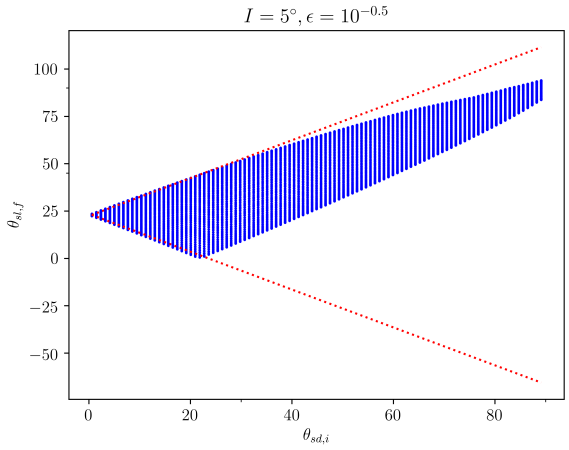

Figure 7. $\theta_f\ (\theta_{sd,i})$ at $\epsilon = 0.3$, firmly in the non-adiabatic regime. Note the clear double-valuedeness has disappeared, as have distinct dynamical histories. The red dotted line presents the analytical prediction given by Equation 18.

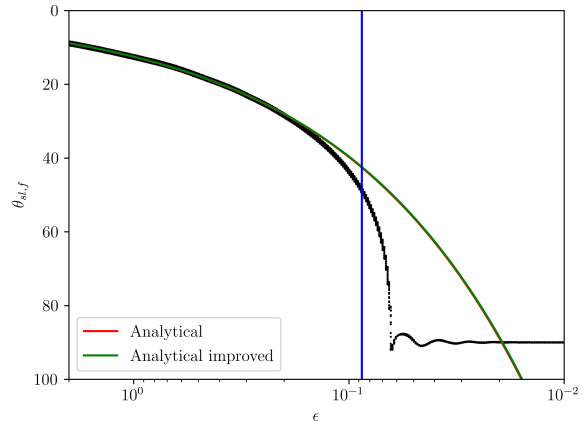

Figure 8. Plot of $\theta_f\ (\theta_{sd,i} = 0)$ as a function of ϵ, where $I = 5°$. Overplotted in the red line is Equation 17, which is in good agreement for $\epsilon \gtrsim 0.1$ the non-adiabatic regime, while $\theta_f \approx 90°$ in the adiabatic regime.

We can naively generalize this by recognizing that any nonzero $\theta_{sd,i}$ manifests as obliquity variations as $\hat{s}$ librates about $\hat{l}_d$, and these oscillations are "frozen in" when the disk dissipates. Thus,

$$\theta_f\ (\theta_{sd,i}) \in \sqrt{\frac{2\pi\Omega}{\epsilon}} \tan I \pm \theta_{sd,i}. \tag{18}$$

We present the results of simulations for using $\epsilon = 0.3$ in Figure 7.

4.3 Transition from Adiabaticity

The agreement of Equation 17 at fixed I for varying ϵ is shown in Figure 8. Note that $\epsilon \to 0$ recovers the adiabatic regime.

An example of an intermediate value $\epsilon = 10^{-2}$ between Figure 5 and Figure 7 is shown in

TODO compare to Equation 13.

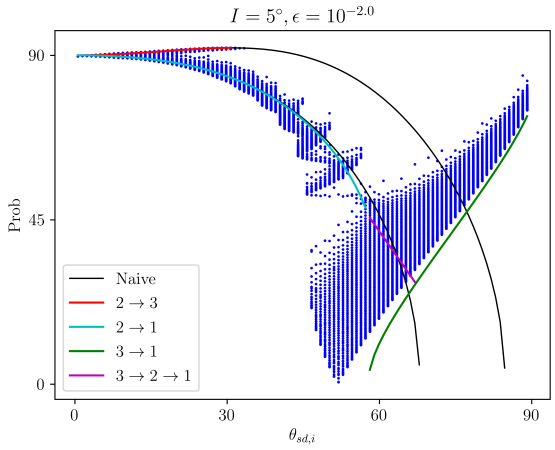

Figure 9. Intermediate ϵ used in between those of Figure 5 and Figure 7. Noticeable "freezing-in" of the obliquity variations over libration cycles is still visible, but the shapes of the adiabatic dynamical trajectories are beginning to appear.

REFERENCES

Anderson K. R., Lai D., 2018, Monthly Notices of the Royal Astronomical Society, 480, 1402
Henrard J., 1982, Celestial Mechanics and Dynamical Astronomy, 27, 3
Henrard J., Murigande C., 1987, Celestial Mechanics, 40, 345
Millholland S., Batygin K., 2019, The Astrophysical Journal, 876, 119
Ward W. R., Hamilton D. P., 2004, The Astronomical Journal, 128, 2501

APPENDIX A: DYNAMICAL HISTORIES

- $A_2 \to A_1$ — Figure 4.
- $A_2 \to A_3$ — Figure A1.
- $A_3 \to A_1$ — Figure A2.
- $A_3 \to A_2 \to A_1$ — Figure A3.
- $A_3 \to A_3$ — Trivial case, the initial enclosed area is too large to ever experience a separatrix encounter.

APPENDIX B: VARIATION WITH I

Plots of Figure 5 but for $I = 10°, I = 20°$.

APPENDIX C: CALCULATION OF TRANSITION PROBABILITIES

Semi-analytic calculation probabilities, including naive line.

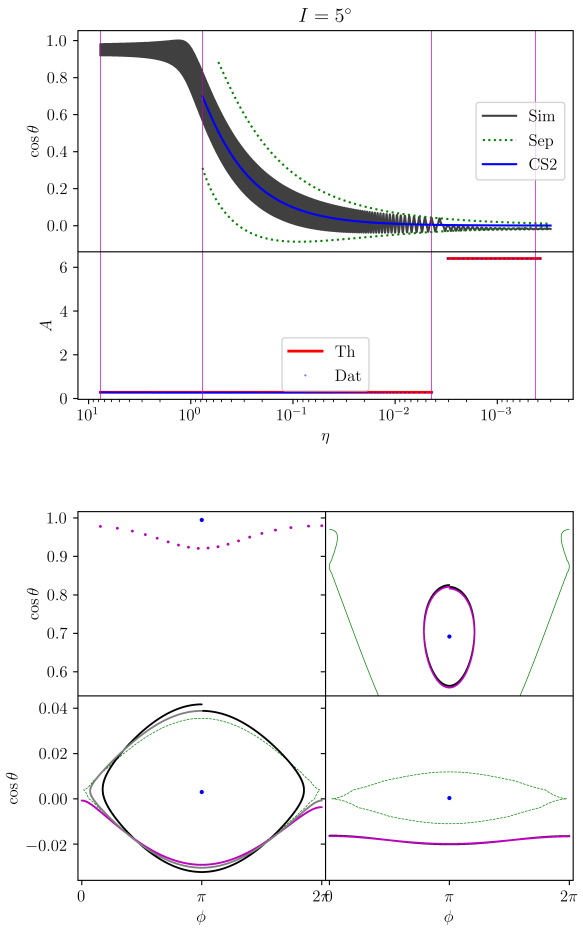

Figure A1. Same as Figure 4 but for the $A_2 \rightarrow A_3$ history.

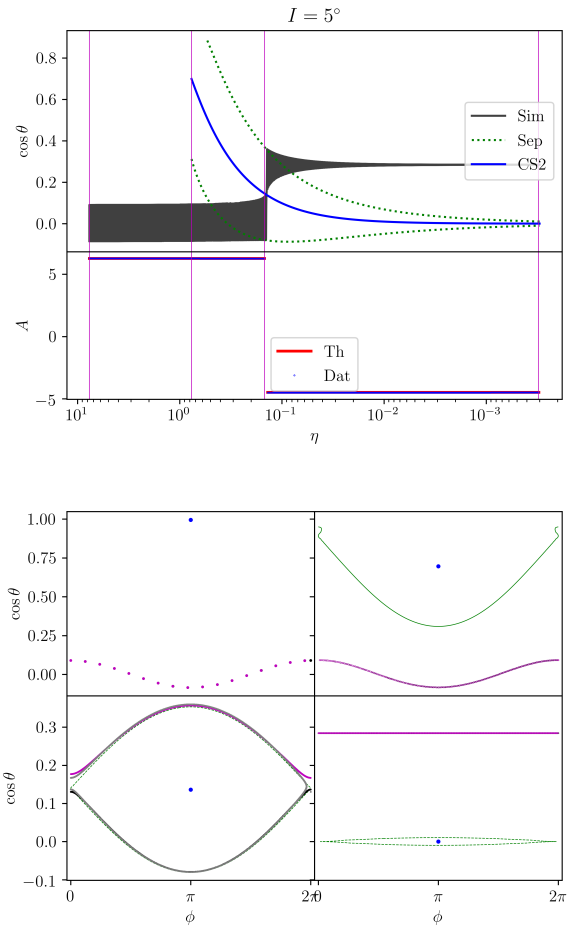

Figure A2. Same as Figure 4 but for the $A_3 \rightarrow A_1$ history. TODO finish final areas plot.

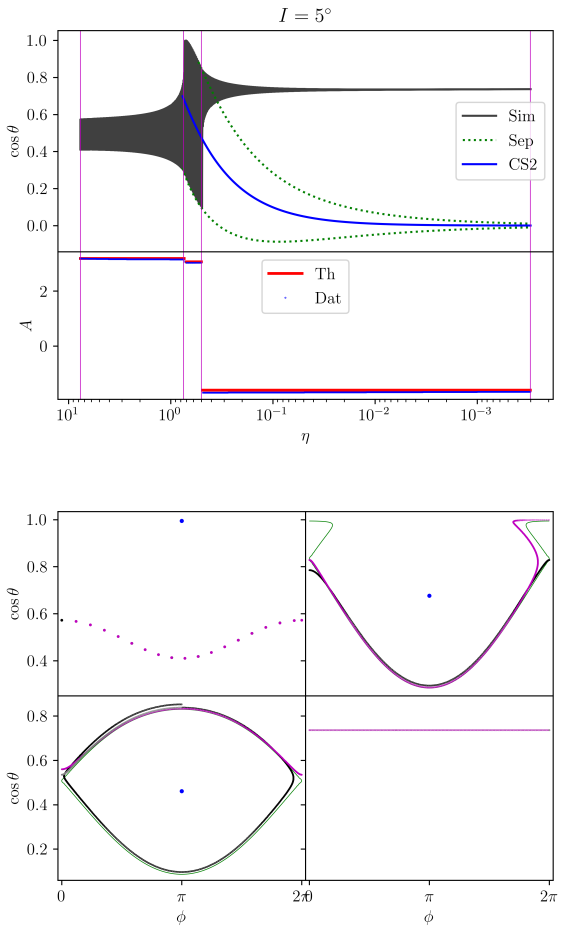

Figure A3. Same as Figure 4 but for the $A_3 \to A_2 \to A_1$ history. The second snapshot, instead of depicting the appearance of the separatrix, captures the first of the two separatrix crossings. TODO finish final areas plot.